




## Imaging the dynamics of initial laser-driven shocks and blowoff plasmas in polystyrene under laser-direct-drive fusion conditions

K. R. P. Kafka <sup>1,\*</sup> S. X. Hu <sup>1,2,3</sup> H. Huang,<sup>1</sup> V. N. Goncharov,<sup>1,2</sup> and S. G. Demos <sup>1</sup>

<sup>1</sup>Laboratory for Laser Energetics, University of Rochester, 250 East River Road, Rochester, New York 14623-1299, USA

<sup>2</sup>Department of Mechanical Engineering, University of Rochester, Rochester, New York 14627, USA

<sup>3</sup>Department of Physics and Astronomy, University of Rochester, Rochester, New York 14627, USA



(Received 23 June 2023; accepted 28 February 2024; published 3 April 2024)

The dynamics of laser-driven shock propagation in solid ablator material, along with the concomitant processes of shinethrough and blowoff plasma plume expansion, at conditions relevant to laser-direct-drive fusion are measured using a tabletop system capable of supporting rapid dataset development with significantly higher resolution compared to existing methods. The experimental results are directly compared with current radiation-hydrodynamic simulations using the two-dimensional code DRACO. Discrepancies between experiments and simulations are evidenced and attributed to limitation of simulation to account for important processes involved in the solid-to-plasma transition.

DOI: [10.1103/PhysRevResearch.6.023013](https://doi.org/10.1103/PhysRevResearch.6.023013)

### I. INTRODUCTION

Inertial confinement fusion (ICF) with a target gain of  $G > 1$  was recently demonstrated following nearly six decades of research and development after its initial conception [1,2]. Achieving ignition (defined as producing more fusion energy than the amount of laser energy delivered to the target) was achieved by the National Ignition Facility [3] using the laser-indirect-drive scheme [4]. This very important step proves that the underlying physics is valid and paves the way toward future inertial fusion energy (IFE) applications. To enable IFE as a viable energy source to humankind, the laser-fusion community generally believes that laser direct drive (LDD) [5] is the right path due to its target simplicity and driving efficiency. A typical LDD target consists of a solid (or liquid) layer of deuterium-tritium encapsulated by a thin layer of ablator material [6–8]. Polystyrene (CH) is often chosen as the ablator material because it is inexpensive and easy to form in spherical targets [9]. Within the context of current ICF experimental configurations utilizing energetic 351-nm laser pulses shining on an LDD target, plasma forms in the dielectric CH target ablator, which is initially transparent to the laser light. How this initial plasma-formation process occurs determines the laser-imprinting level (due to transverse laser-intensity nonuniformity on the target), which provides the initial seeds for the Rayleigh-Taylor instability growth during the LDD target implosion [10–21].

LDD studies have largely overlooked this intricate process of initial plasma formation, partially due to the lack of suitable plasma-imaging techniques. Recent experimental evidence suggests that the failure to consider this initial plasma formation might have caused a discrepancy between radiation-hydrodynamic simulations and experimental measurements using the OMEGA high-resolution velocimeter [22]. To fill this gap in understanding, multiple models for the initial plasma-formation process have been derived [23–25], several of which have been benchmarked by one-dimensional transmission measurements [26]. Such plasma-formation models, however, have not yet been implemented into radiation-hydrodynamic simulations. Regardless of initial plasma formation, it is well understood that laser imprinting is at least a 2D process; that is, the nonuniform laser-intensity distribution on the target surface will translate to perturbed shocks and driving-pressure nonuniformity. Thus, the experimental 2D mapping of the laser-driven shock and the blowoff coronal plasmas will provide valuable inputs for benchmarking laser-imprinting models.

To develop a capability for mapping as stated above, we have conducted pump-probe imaging experiments using a tabletop platform that mimics the initial LDD plasma-formation conditions. The experiments measure not only the dynamics of laser-driven shock propagation in solid CH with significantly higher resolution compared to VISAR (velocity interferometer system for any reflector), but also the preceding material modification due to shinethrough (i.e., before the formation of critical plasma on the surface) and the coronal plasma formation and expansion. These results are compared with standard radiation-hydrodynamic simulations, which currently do not take the initial plasma-formation process into account; the resultant differences shall motivate the implementation of models of initial plasma formation into future simulations. The experimental results also provide direct measurement of the initial differences in shock propagation

\*kkaf@lle.rochester.edu

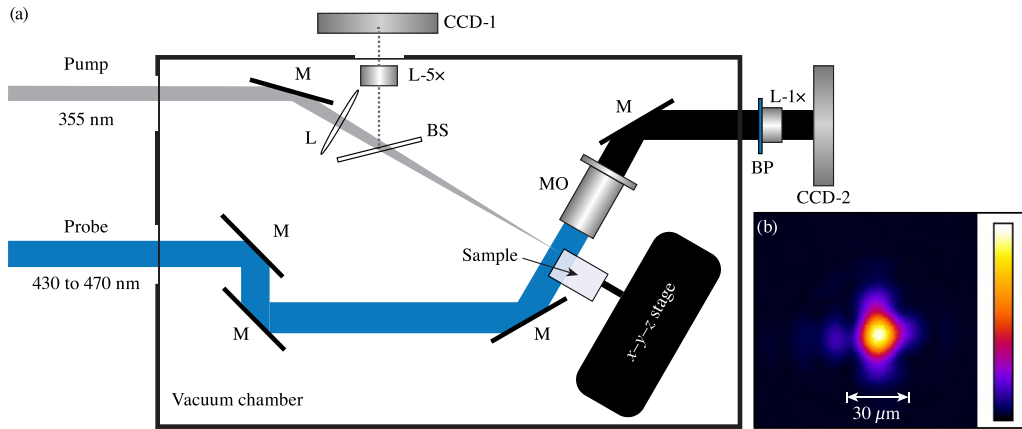


FIG. 1. (a) Schematic diagram of the experimental system and (b) spatial profile of the pump beam in the target plane. M: mirror; L: lens; BS: beam splitter; CCD-1: beam profiler; CCD-2: probe-imaging camera; MO: microscope objective; BP: bandpass filter.

and time of formation of critical plasma arising from laser-intensity nonuniformity on target—the critical mechanisms of laser imprint. The objective of this work is to provide the necessary data to benchmark physics-based multidimensional models of laser imprinting for better LDD target designs and understanding.

## II. EXPERIMENTAL ARRANGEMENT

The experiments are performed using a custom-designed optical parametric chirped-pulse-amplification (OPCPA) laser system (manufactured by EKSPLA) providing a temporally synchronized dual-beam output of 100-ps, 355-nm pulses and 20-fs, 900-nm pulses. The 100-ps pulse, which serves as a pump pulse for experiments, is obtained by diverting a fraction of the pump laser of the OPCPA system into a diode-pumped amplifier, and subsequently generating its third harmonic (355 nm) with a maximum pulse energy of about 100 mJ. The experimental probe pulse is produced by second-harmonic generation of the 20-fs pulse into a subpicosecond-duration pulse centered at 450 nm. As a result of this laser architecture, the pump and probe pulses are temporally synchronized and have an estimated jitter of the order of  $\sim 1$  ps or less, making it possible to measure the dynamic processes involved during the pump pulse with adequate temporal resolution.

A schematic layout of the experimental station is depicted in Fig. 1. The 355-nm pump pulse is focused onto the sample at normal incidence inside a vacuum chamber (about  $10^{-5}$  torr) with peak intensity on the sample up to  $\sim 5 \times 10^{13}$  W/cm<sup>2</sup>. The pump focal spot is characterized by diverting a fraction of the converging pump beam with a beam splitter and capturing the image of the beam at the sample-surface equivalent plane onto a beam profiling charge-coupled device camera (CCD-1) following  $5\times$  optical magnification ( $L-5\times$ ). The pump-beam spot size used in the experiments is  $30\ \mu\text{m}$  in diameter [see beam profile in Fig. 1(b)] attained using an  $f/20$  focusing geometry by a 30-cm lens.

The time-resolved dynamics of the sample's material response (bulk shock wave, plasma expansion, etc.) are imaged using the probe pulse as strobe illumination after it passes through a variable optical delay line. The collimated probe

beam is aligned at grazing incidence to the sample surface to provide images of the internal or external interaction regions of interest and to measure shock-wave characteristics and the plume expansion, respectively. The interaction is imaged using a long-working-distance (Mitutoyo)  $10\times$  microscope objective located within the vacuum chamber, aligned perpendicular to the pump beam. The images are then transported and captured on an external CCD camera (CCD-2) via a tube lens ( $L-1\times$ ) and a  $450 \pm 5$ -nm narrow-band filter to limit contribution on the image by the generated plasma emission. For experiments with probe angle of incidence  $< 90^\circ$ , a physical mask (not shown) is used to block the directly transmitted beam, thereby preventing interference fringes from being generated due to the geometry.

The image acquisition is performed at 5 Hz and synchronized with the probe pulse. The sample is exposed to only one pump pulse per measurement using a computer controlled shutter. To improve image quality, each probe image collected during the event is normalized taking its ratio to an image captured before the pump pulse arrives. For experiments requiring variation of peak intensity, a wave plate and polarizer located outside the vacuum chamber were used to attenuate the pump-pulse energy by up to about two orders of magnitude without altering the temporal and spatial characteristics of the pump pulse on the target.

The samples were prepared from bulk polystyrene blocks (Goodfellow Corp.) that were cut to the dimensions of  $10 \times 2 \times 1.2$  cm, each optically polished in-house on the four large surfaces. Samples were positioned with the pump beam incident on a  $10 \times 1.2$ -cm face, about 1 mm from the long edge nearest the microscope objective (see Fig. 1). This positioning was selected to ensure that the resolution of the microscope, when imaging inside the sample, is not hampered by imaging too deep into the bulk (i.e., observable image degradation appears at  $\sim 2$ -mm depth). After each pump pulse, the sample was translated by  $300\ \mu\text{m}$  to a pristine site along its 10-cm (vertical) axis. The strobe-illumination probe beam propagates through a vacuum window and along the shortest dimension of the sample (1.2 cm), and even though the probe pulse is significantly stretched by dispersive propagation, the estimated pulse duration is still  $< 1$  ps (measured 300 fs before entering polystyrene). This provides sufficiently high

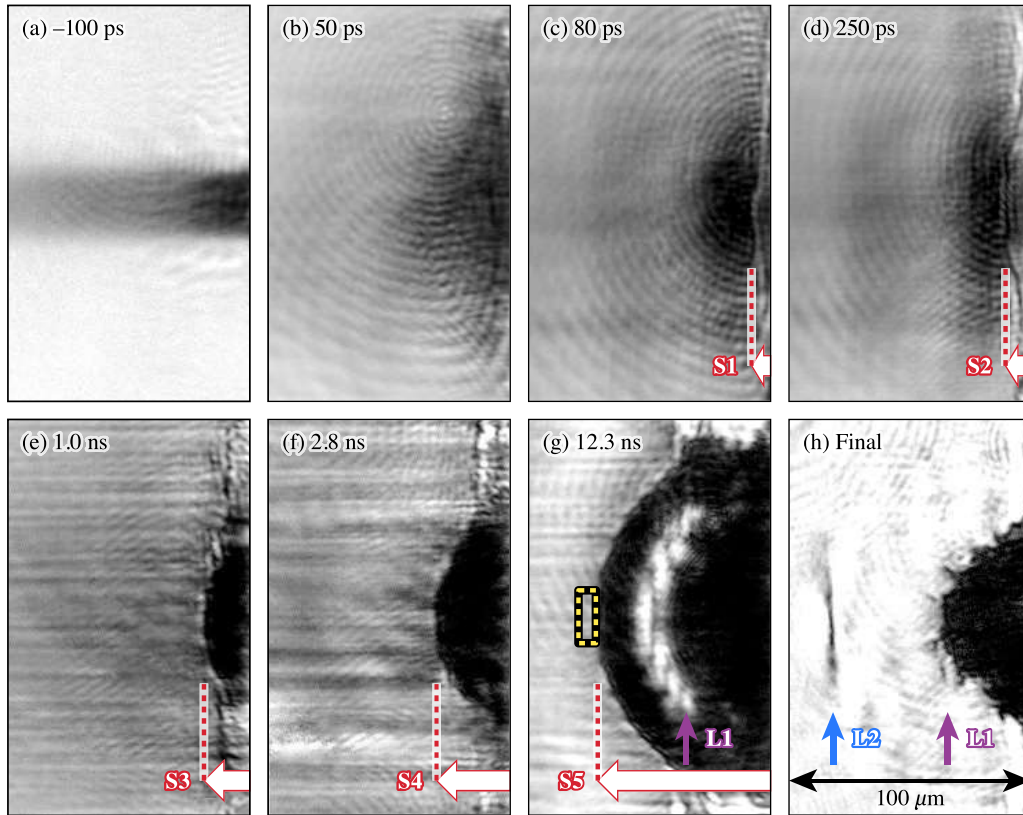


FIG. 2. Probe ratio images inside the polystyrene sample at indicated delay times, all on the same length scale. The right edge of each image is located at the polystyrene-vacuum interface. The intensity is displayed on (a) a linear scale, while all others [(b)–(h)] are on a logarithmic scale to enhance visibility of the features of interest. Red arrows and dashed lines ( $S_n$ ) are a guide to the eye to the observed shock depth. Arrows indicate the crater depth ( $L_1$ ) and plastic deformation depth ( $L_2$ ). Dashed-yellow box indicates example region used to obtain transmission values shown in Fig. 3.

temporal resolution to resolve hydrodynamic processes, such as material shock propagation and plume expansion, via direct imaging. We note, however, that both the shock and the plume cannot be observed simultaneously because of a mismatch in optical thickness between the polystyrene and vacuum (i.e., different “apparent depths”). Thus, different experiments were performed for each case.

### III. EXPERIMENTAL RESULTS AND DISCUSSION

The aim of the experiments was to resolve the dynamics of three key processes that are believed to be related to the laser-imprinting process and lead to reduced performance of target implosions in LDD fusion experiments. These include (1) the quantification of the “laser shinethrough” effect, (2) the accurate measurement of the shock-wave propagation inside the material, including both position and speed, and (3) the characteristics of the blowoff plasma and plume expansion.

Example images captured inside the polystyrene bulk are shown in Fig. 2 at different time delays from the peak of the pump pulse ( $5 \times 10^{13} \text{ W/cm}^2$ ). The right edge of each image in Fig. 2 corresponds to the polystyrene-vacuum interface. The time-resolved image shown in Fig. 2(a) was captured at a  $-100$ -ps delay (i.e., 100 ps before the peak of the pump pulse) and represents the first type of observable material modification (occurring about  $20 \pm 10$  ps before critical

plasma density is reached at the input surface) manifested as a darker region resulting from the localized absorption of the probe beam. This induced absorption is first observed at the region exposed to peak pump intensity (about  $22 \mu\text{m}$  wide) and is attributed to the buildup of the electron population inside the material (subcritical density plasma) until the critical plasma is formed on the surface to terminate this process. The radius of this absorbing region increases (vertical dimension in Fig. 2) with increasing delay time due to the spatial distribution of the beam intensity (approximately Gaussian) since initiating subcritical plasma requires longer delays as local beam intensity decreases (see also discussion related to Fig. 6).

The subcritical plasma excitation was observed to extend  $>1 \text{ mm}$  into the bulk, indicating significant shinethrough energy penetrating the material. This effect can cause target preheating in LDD, given that typical fusion targets employing CH ablator materials (such as polystyrene) have a thickness of  $<10 \mu\text{m}$ . The analysis of images captured at different delays enables the characterization of the relaxation time of the electronic excitation, with the result shown in Fig. 3 indicating the average value of the probe transmission at a depth of  $76 \mu\text{m}$  from the sample surface [dashed-yellow box region in Fig. 2(g)]. This depth is located just beyond the maximum extent of the shock front at the longest measured delay time in this experiment, thus allowing characterization

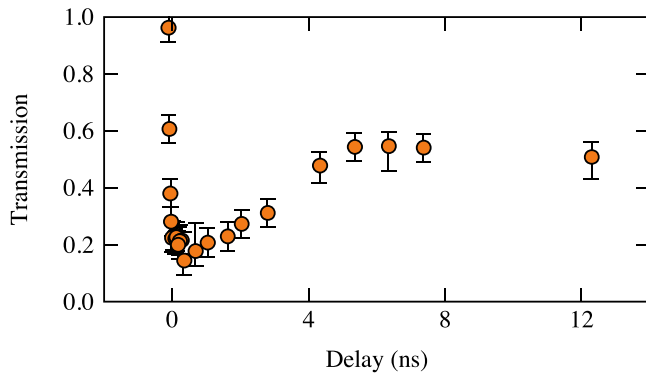


FIG. 3. Average probe transmission value at a 76- $\mu\text{m}$  depth from the surface as a function of delay, indicating the characteristic relaxation timescales of the excited volume.

of the excitation/relaxation across all measured delays. As seen in Fig. 3, the transmission drops rapidly to a minimum value of about 0.2, recovers to about 0.5 within 5 ns, and then remains constant, indicating the presence of an additional relaxation component(s) having much longer relaxation time. Therefore, two characteristic lifetimes are observed: a 5-ns component and a longer-lived component that exhibited negligible relaxation within the 12-ns maximum delay time used in this work. The 5-ns component is of the same order as the reported fluorescence lifetime in polystyrene [27] and is therefore attributed to electron relaxation. This set of measurements captures in detail the ensuing material response to the phenomenon termed laser shinethrough [28,29], namely, the transient excitation of the material preceding the formation of critical plasma near the surface.

The shortest delay times at which the observation of the shock-wave expansion inside the CH material was well defined was near the end of the pump pulse at about an 80-ps delay [Fig. 2(c)], but was not yet discernible at the 50-ps delay [Fig. 2(b)]. This is attributed to the complex optical properties of the material occurring during the plasma initiation process in combination with their spatial scale that approaches the spatial resolution of the imaging system. Specifically, the absorption and refraction of the probe beam within the excited volume is determined by the three-dimensional (3D) refractive index distribution corresponding to the distributions of plasma density, pressure, and temperature, which in turn are functions of the spatiotemporal profile of the pump laser. For delays after the termination of the pump pulse, the location of the propagating shock front is well defined, as demonstrated by example images at different delay times shown in Figs. 2(b)–2(g) (displayed on a logarithmic intensity scale to improve contrast). Although the appearance and relative contrast of the shock front image varies slightly with delay time, arguably due to the distortions to the probe-beam propagation caused by the complex transient material properties, its evolution is clearly observed in the time-resolved images. The final morphology of the material shown in Fig. 2(h) includes a crater (of depth L1) and another induced material boundary at a deeper depth (L2) that reasonably corresponds to the transition from plastic to elastic deformation of the material in response to the pressure pulse [30], i.e., the position where the shock has decayed to a sound wave.

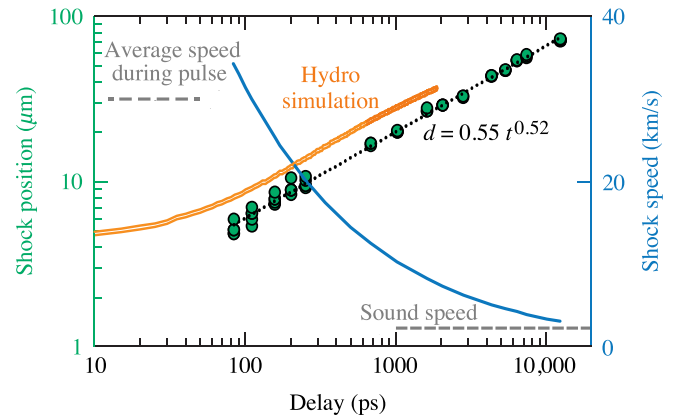


FIG. 4. Measured position of the shock front (circles) as a function of delay after pump-pulse peak intensity, with power-law fit (dotted line) and corresponding simulation results (double line). Speed of the shock front (solid line) that is implied by the measured positions, with average speed during the pump pulse indicated (dashed line). The sound speed (dashed-dotted line) is included for comparison.

Comparing this final morphology to the image of the shock with sufficiently long delays indicates that the signature of the ablation-crater boundary is formed at delays shorter than 10 ns. For example, the image in Fig. 2(g) represents a superposition of the features of the shock wave (S5) and the formed volume of superheated material (L1) that is ejected to form the crater at later times. The latter is observed as the region nearest the surface (right side) that approximately corresponds to the final size of the crater. Regarding other features in Fig. 2, horizontal striations are visible in the unshocked regions of the bulk and remain visible for the entirety of the delays measured in this work. The cause of these striations is unknown but we hypothesize that it may be related to the onset of pump-beam filamentation or probe refraction through the temperature and pressure distribution introduced by the pump. The curved ripples are imaging artifacts resulting from diffraction in the optical system and should be ignored.

The location of the shock front as a function of delay is plotted in Fig. 4 on a log-log scale with each data point corresponding to the measured value from individual time-resolved images. A power-law fit overlaps the data reasonably well with an exponent of  $\sim 0.5$ . Since the smallest average measured value of the shock position at the end of the laser pulse (80-ps delay) is about 5  $\mu\text{m}$  from the sample's surface, the unknown earlier time coordinates introduce an uncertainty into the fit exponent of  $\sim \pm 0.05$ . The speed as a function of delay is calculated by taking the derivative of the fit equation. The corresponding speed values vary from 34 km/s to 3 km/s across the range of delays where a shock was observed, from 80 ps to 12.3 ns delays, respectively. We also include the estimated value of the average speed of 30 km/s during the laser pulse, calculated using the earliest measured shock depth divided by the time duration from the formation of the critical plasma (determined based on the results of the earliest observed ablation discussed later). The speeds presented here are similar to VISAR measurements [31], and are observed to be measurable at slightly earlier delay times.

VISAR measurements do not, however, provide information on the position of the shock wave while their spatial resolution is of the order of  $10\ \mu\text{m}$ . We thus consider the present method more suitable for validating and improving modeling tools.

A radiation-hydrodynamic simulation with DRACO [32] was used to simulate the same conditions probed by the experiments. DRACO is a 2D radiation-hydrodynamics code for simulating and designing direct-drive ICF targets, and is initialized with a so-called “cold start” where the initial target capsule is assumed to be in overcritical plasma state. Primary known potential deviations of modeling from actual physics include (1) that the solid-to-plasma transition effects are absent from the modeling (i.e., critical plasma formation is assumed to be instantaneous), (2) that shinethrough is not considered, and (3) that laser deposition starts at the target surface. The DRACO simulations of the shock position as a function of time are compared with the experimental data shown in Fig. 4. These results indicate that the simulations consistently overestimate the position of the shock inside the ablator material. Note that the data are on a log-log scale, so the discrepancy between simulation and experiment cannot simply be resolved by a constant shift of the data. Given that the simulations do not incorporate a solid-to-plasma transition, these results may suggest that the dynamics and/or depth of initial plasma formation used in the hydrocode do not match experiments. This may imply that the transition from cold solid to plasma results in a reduced peak pressure within the formed critical plasma zone, thereby giving a retarded location of the shock in reality.

The method used for shock imaging was also applied to observe the dynamics of the blowoff coronal plasma that expands away from the material surface. There are various configurations at which such images can be acquired, including varying the angle of illumination and the focus plane of the imaging system. Example images for a pump peak intensity of  $5 \times 10^{13}\ \text{W}/\text{cm}^2$  are shown in Figs. 5(a) and 5(b), and were captured at the same delay but at slightly different probe-imaging configurations. Figure 5(a) displays the plume with the probe beam aligned to a  $90^\circ$  angle of incidence (parallel to surface) and provides a clear outline of the plume front, which is defined as the location in the image where direct probe-light propagation (uniform background) is altered (white arrow and dashed line). The image in Fig. 5(b) was obtained with the probe angle of incidence slightly reduced (to about  $85^\circ$ ); a dark region nearer to the surface is observed [location shown with the solid arrow and dashed line in Fig. 5(b)]. Bright fringes in the outer region, however, cause the interpretation of the plume-front position to be more difficult to accurately define. Nonetheless, the experiments were performed using both configurations. The images were analyzed across a range of delays and the results are plotted in Fig. 5(c). The onset of the expanding plume is first observed at  $-70\ \text{ps}$  delay, while no detectable modification was observed at  $-80\ \text{ps}$  delay. Since separate transmission measurements (see discussion of Fig. 6) suggest formation of the critical plasma no earlier than  $-90\ \text{ps}$ , we conclude that the critical plasma was formed at about  $-80\ \text{ps}$ . During and immediately after the pump pulse, the plume front expands with an approximately constant speed of about  $350\ \text{km}/\text{s}$ . The speed of expansion of the dark region within the plume was also measured and found to exhibit

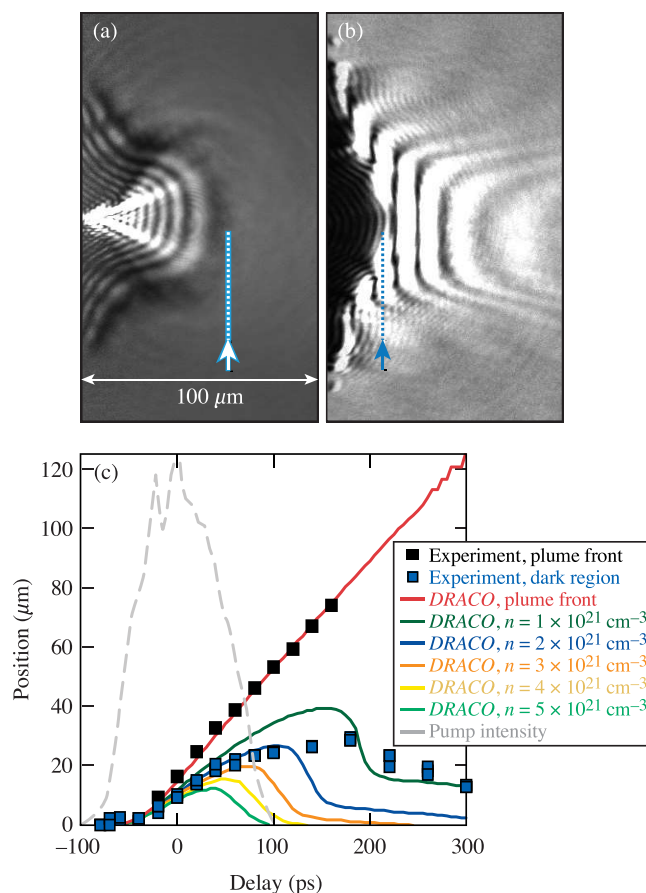


FIG. 5. Probe ratio images and analysis of the plume expanding into vacuum, where the left edge of the images corresponds to the polystyrene-vacuum interface. Both images are equivalently at a 100-ps delay, imaged with the probe beam at (a)  $90^\circ$  incidence and (b)  $\sim 85^\circ$  incidence. The arrows and dashed lines in the images indicate the corresponding features plotted in (c), which are the positions of the dark region front and plume front as a function of delay, along with the corresponding DRACO simulation results for different plasma densities. The normalized pump intensity is overlaid for reference.

maximum value of  $220\ \text{km}/\text{s}$ , but its expansion is halted at about  $180\ \text{ps}$  delay and subsequently recedes.

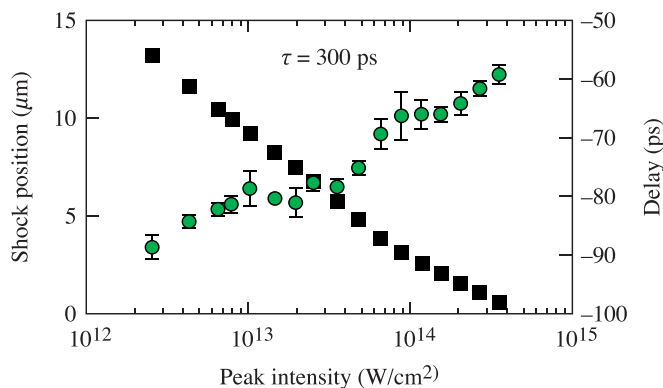


FIG. 6. Shock position (green circles) at a fixed 300-ps delay as a function of pump peak intensity, and the inferred critical plasma initiation time (black squares).

The DRACO simulation results are shown by solid lines in Fig. 5(c) along with the experimental results (data points) to facilitate direct comparison. The plume-front position is consistent between experiment and simulation. On the other hand, the location of the boundary of the dark region appears to correspond to about  $(1-2) \times 10^{21} \text{ cm}^{-3}$  from the simulations, which is less than the critical plasma density for the probe wavelength of about  $5 \times 10^{21} \text{ cm}^{-3}$ . Using the spatial distribution of the electron density of the blowoff corona plasma obtained from DRACO simulations at different delay times, ray-tracing modeling was performed to explore the origin of the observed dark region. The results suggest that this feature can arise not only from the presence of critical plasma (preventing propagation of the light), but also due to the refraction of probe beam rays as they propagate through the subcritical plasma region (which exhibits a 3D varying index of refraction). As a result, reconstruction of the electron density distribution in the blowoff plasma is not trivial, and this outer boundary of the dark region does not coincide with that of the critical plasma density. Future work will focus on developing reconstruction methods using images acquired with varying focus planes and angles of incidence.

All of the data presented up to this point were taken at a fixed peak intensity of the pump ( $5 \times 10^{13} \text{ W/cm}^2$ ). Given that the instantaneous spatial profile of the focused picket pulse in direct-drive fusion experiments can be speckled, which may lead to phase instabilities, measurements of the dynamics as a function of peak pump intensity were performed. For these measurements, the pump was focused to a smaller spot (16  $\mu\text{m}$  in diameter), yielding peak intensity up to about  $4 \times 10^{14} \text{ W/cm}^2$ . Figure 6 shows the position of the shock inside the material at a fixed delay of 300 ps as a function of the pump-pulse peak intensity. This delay was chosen to ensure that the shock position is detected even for the lower pump intensities. The results show that, over the range of measured peak intensity change by a factor of about 100, the shock position (and corresponding average shock propagation speed) changes by about a factor of 3. If we limit that range to a change in intensity by a factor of 10 from peak intensity, the shock propagation average speed changes by a factor of about 2, which can seed phase instabilities.

Analysis of data empirically suggests that the critical plasma is formed once a dose of  $8 \pm 2 \text{ J/cm}^2$  is accumulated on the sample, independent of the pump-pulse peak intensity over a factor of about  $10^3$  change in peak intensity ( $5 \times 10^{10}$  to  $5 \times 10^{13} \text{ W/cm}^2$ ). This agrees with previous work that also suggested that the shinethrough energy is approximately constant as a function of peak intensity [28]. The dependence

depicted in Fig. 6 shows the inferred delay time for critical plasma initiation as a function of the laser peak intensity. Considering an approximate factor of 10 between “hot” and “cold” spots in fusion laser spatial profiles, the speckle pattern leads to a 20-ps delay of critical plasma formation. Consequently, this can also be a mechanism for initiating perturbations in the formed plasma that can lead to laser imprinting.

In summary, we have performed tabletop pump-probe experiments to image the shock formation and blowoff plasma dynamics that are closely related to the starting (laser-imprinting) conditions of LDD fusion experiments. Discrepancies between experiments and simulations are evidenced by the difference in the dynamics of shock formation, which is initiated earlier in DRACO due to the neglect of the solid-to-plasma transition process in current code. Results also quantify the difference of shock dynamics inside the material as a function of local laser intensity, which can be the source of initiation of plasma instabilities. The method presented in this work, based on a tabletop system, is capable of rapidly producing large datasets, and along with future refinements it is expected to support improvement of laser-imprinting modeling for reliable LDD target designs and simulations.

#### ACKNOWLEDGMENTS

The authors thank Alexander Maltsev for fabricating the optically polished polystyrene samples, and John Lambropoulos for fruitful discussions regarding plastic deformation. This material is based upon work supported by the Department of Energy National Nuclear Security Administration under Award No. DE-NA0003856, the University of Rochester, and the New York State Energy Research and Development Authority.

This report was prepared as an account of work sponsored by an agency of the U.S. Government. Neither the U.S. Government nor any agency thereof, nor any of their employees, makes any warranty, express or implied, or assumes any legal liability or responsibility for the accuracy, completeness, or usefulness of any information, apparatus, product, or process disclosed, or represents that its use would not infringe privately owned rights. Reference herein to any specific commercial product, process, or service by trade name, trademark, manufacturer, or otherwise does not necessarily constitute or imply its endorsement, recommendation, or favoring by the U.S. Government or any agency thereof. The views and opinions of authors expressed herein do not necessarily state or reflect those of the U.S. Government or any agency thereof.

[1] J. Nuckolls, L. Wood, A. Thiessen, and G. Zimmerman, Laser compression of matter to super-high densities: Thermonuclear (CTR) applications, *Nature (London)* **239**, 139 (1972).  
 [2] H. Abu-Shawareb, R. Acree, P. Adams, J. Adams, B. Addis, R. Aden, P. Adrian, B. B. Afeyan, M. Aggleton, L. Aghaian *et al.* (Indirect Drive ICF Collaboration), Lawson criterion for ignition exceeded in an inertial fusion experiment, *Phys. Rev. Lett.* **129**, 075001 (2022).

[3] E. M. Campbell and W. J. Hogan, The National Ignition Facility—applications for inertial fusion energy and high-energy-density science, *Plasma Phys. Control. Fusion* **41**, B39 (1999).  
 [4] S. W. Haan, J. D. Lindl, D. A. Callahan, D. S. Clark, J. D. Salmonson, B. A. Hammel, L. J. Atherton, R. C. Cook, M. J. Edwards, S. Glenzer *et al.*, Point design targets, specifications, and requirements for the 2010 ignition campaign on the National Ignition Facility, *Phys. Plasmas* **18**, 051001 (2011).

- [5] R. S. Craxton, K. S. Anderson, T. R. Boehly, V. N. Goncharov, D. R. Harding, J. P. Knauer, R. L. McCrory, P. W. McKenty, D. D. Meyerhofer, J. F. Myatt *et al.*, Direct-drive inertial confinement fusion: A review, *Phys. Plasmas* **22**, 110501 (2015).
- [6] V. N. Goncharov, T. C. Sangster, T. R. Boehly, S. X. Hu, I. V. Igumenshchev, F. J. Marshall, R. L. McCrory, D. D. Meyerhofer, P. B. Radha, W. Seka *et al.*, Demonstration of the highest deuterium-tritium areal density using multiple-picket cryogenic designs on OMEGA, *Phys. Rev. Lett.* **104**, 165001 (2010).
- [7] S. X. Hu, V. N. Goncharov, P. B. Radha, J. A. Marozas, S. Skupsky, T. R. Boehly, T. C. Sangster, D. D. Meyerhofer, and R. L. McCrory, Two-dimensional simulations of the neutron yield in cryogenic deuterium-tritium implosions on OMEGA, *Phys. Plasmas* **17**, 102706 (2010).
- [8] V. N. Goncharov, S. P. Regan, E. M. Campbell, T. C. Sangster, P. B. Radha, J. F. Myatt, D. H. Froula, R. Betti, T. R. Boehly, J. A. Delettrez *et al.*, National direct-drive program on OMEGA and the National Ignition Facility, *Plasma Phys. Control. Fusion* **59**, 014008 (2017).
- [9] S. X. Hu, L. A. Collins, T. R. Boehly, Y. H. Ding, P. B. Radha, V. N. Goncharov, V. V. Karasiev, G. W. Collins, S. P. Regan, and E. M. Campbell, A review of *ab initio* studies of static, transport, and optical properties of polystyrene under extreme conditions for inertial confinement fusion applications, *Phys. Plasmas* **25**, 056306 (2018).
- [10] S. E. Bodner, Rayleigh–Taylor instability and laser-pellet fusion, *Phys. Rev. Lett.* **33**, 761 (1974).
- [11] R. Ishizaki and K. Nishihara, Propagation of a rippled shock wave driven by nonuniform laser ablation, *Phys. Rev. Lett.* **78**, 1920 (1997).
- [12] S. P. Obenschain, D. G. Colombant, M. Karasik, C. J. Pawley, V. Serlin, A. J. Schmitt, J. L. Weaver, J. H. Gardner, L. Phillips, Y. Aglitskiy *et al.*, Effects of thin high-Z layers on the hydrodynamics of laser-accelerated plastic targets, *Phys. Plasmas* **9**, 2234 (2002).
- [13] S. Fujioka, A. Sunahara, K. Nishihara, N. Ohnishi, T. Johzaki, H. Shiraga, K. Shigemori, M. Nakai, T. Ikegawa, M. Murakami *et al.*, Suppression of the Rayleigh–Taylor instability due to self-radiation in a multiablation target, *Phys. Rev. Lett.* **92**, 195001 (2004).
- [14] L. Masse, Stabilizing effect of anisotropic thermal diffusion on the ablative Rayleigh–Taylor instability, *Phys. Rev. Lett.* **98**, 245001 (2007).
- [15] V. A. Smalyuk, S. X. Hu, J. D. Hager, J. A. Delettrez, D. D. Meyerhofer, T. C. Sangster, and D. Shvarts, Rayleigh–Taylor growth measurements in the acceleration phase of spherical implosions on OMEGA, *Phys. Rev. Lett.* **103**, 105001 (2009).
- [16] S. Depierreux, C. Labaune, D. T. Michel, C. Stenz, P. Nicolai, M. Grech, G. Riazuelo, S. Weber, C. Riconda, V. T. Tikhonchuk *et al.*, Laser smoothing and imprint reduction with a foam layer in the multikilojoule regime, *Phys. Rev. Lett.* **102**, 195005 (2009).
- [17] S. X. Hu, G. Fiksel, V. N. Goncharov, S. Skupsky, D. D. Meyerhofer, and V. A. Smalyuk, Mitigating laser imprint in direct-drive inertial confinement fusion implosions with high-Z dopants, *Phys. Rev. Lett.* **108**, 195003 (2012).
- [18] M. Karasik, J. L. Weaver, Y. Aglitskiy, J. Oh, and S. P. Obenschain, Suppression of laser nonuniformity imprinting using a thin high-Z coating, *Phys. Rev. Lett.* **114**, 085001 (2015).
- [19] S. X. Hu, D. T. Michel, A. K. Davis, R. Betti, P. B. Radha, E. M. Campbell, D. H. Froula, and C. Stoeckl, Understanding the effects of laser imprint on plastic-target implosions on OMEGA, *Phys. Plasmas* **23**, 102701 (2016).
- [20] D. T. Michel, S. X. Hu, A. K. Davis, V. Yu. Glebov, V. N. Goncharov, I. V. Igumenshchev, P. B. Radha, C. Stoeckl, and D. H. Froula, Measurement of the shell decompression in direct-drive inertial-confinement-fusion implosions, *Phys. Rev. E* **95**, 051202(R) (2017).
- [21] S. X. Hu, W. Theobald, P. B. Radha, J. L. Peebles, S. P. Regan, A. Nikroo, M. J. Bonino, D. R. Harding, V. N. Goncharov, N. Petta *et al.*, Mitigating laser-imprint effects in direct-drive inertial confinement fusion implosions with an above-critical-density foam layer, *Phys. Plasmas* **25**, 082710 (2018).
- [22] J. L. Peebles, S. X. Hu, W. Theobald, V. N. Goncharov, N. Whiting, P. M. Celliers, S. J. Ali, G. Duchateau, E. M. Campbell, T. R. Boehly *et al.*, Direct-drive measurements of laser-imprint-induced shock velocity nonuniformities, *Phys. Rev. E* **99**, 063208 (2019).
- [23] G. Duchateau, S. X. Hu, A. Pineau, A. Kar, B. Chimier, A. Casner, V. Tikhonchuk, V. N. Goncharov, P. B. Radha, and E. M. Campbell, Modeling the solid-to-plasma transition for laser imprinting in direct-drive inertial confinement fusion, *Phys. Rev. E* **100**, 033201 (2019).
- [24] A. Kar, S. X. Hu, G. Duchateau, J. Carroll-Nellenback, and P. B. Radha, Implementing a microphysics model in hydrodynamic simulations to study the initial plasma formation in dielectric ablator materials for direct-drive implosions, *Phys. Rev. E* **101**, 063202 (2020).
- [25] A. Pineau, B. Chimier, S. X. Hu, and G. Duchateau, Improved modeling of the solid-to-plasma transition of polystyrene ablator for laser direct-drive inertial confinement fusion hydrocodes, *Phys. Rev. E* **104**, 015210 (2021).
- [26] A. Pineau, K. R. P. Kafka, S. G. Demos, T. Z. Kosci, V. N. Goncharov, S. X. Hu, and G. Duchateau, Benchmarking solid-to-plasma transition modeling for inertial confinement fusion laser-imprint with a pump-probe experiment, *Phys. Rev. Res.* **4**, 033178 (2022).
- [27] L. J. Basile, Effect of styrene monomer on the fluorescence properties of polystyrene, *J. Chem. Phys.* **36**, 2204 (1962).
- [28] D. K. Bradley, T. Boehly, D. L. Brown, J. Delettrez, W. Seka, and D. Smith, Early-time ‘shine-through’ in laser-irradiated targets, in *Laser Interaction and Related Plasma Phenomena*, edited by H. Hora and G. Miley (Plenum, New York, 1991), Vol. 9, p. 323.
- [29] D. H. Edgell, W. Seka, R. E. Bahr, T. R. Boehly, and M. J. Bonino, Effectiveness of silicon as a laser shine-through barrier for 351-nm light, *Phys. Plasmas* **15**, 092704 (2008).
- [30] R. Hill, *The Mathematical Theory of Plasticity* (Clarendon, Oxford, 1950).
- [31] T. R. Boehly, E. Vianello, J. E. Miller, R. S. Craxton, T. J. B. Collins, V. N. Goncharov, I. V. Igumenshchev, D. D. Meyerhofer, D. G. Hicks, P. M. Celliers *et al.*, Shock-timing experiments using double-pulse laser irradiation, *Phys. Plasmas* **13**, 056303 (2006).
- [32] P. B. Radha, T. J. B. Collins, J. A. Delettrez, Y. Elbaz, R. Epstein, V. Yu. Glebov, V. N. Goncharov, R. L. Keck, J. P. Knauer, J. A. Marozas *et al.*, Multidimensional analysis of direct-drive, plastic-shell implosions on OMEGA, *Phys. Plasmas* **12**, 056307 (2005).